PHYSICAL REVIEW MATERIALS **7**, 014803 (2023)

Ultrathin epitaxial MgB_2 on SiC: Substrate surface-polarity-dependent properties

Weibing Yang,[1,†,*] Leila Kasaei,[2,†] Hussein Hijazi,[2] Sylvie Rangan,[2] Yao-wen Yeh,[2] Raj K. Sah,[1] Jay R. Paudel,[1]
Ke Chen,[1] Alexander X. Gray,[1] Philip Batson,[2] Leonard C. Feldman,[2] and Xiaoxing Xi[1]
[1]*Department of Physics, Temple University, Philadelphia, Pennsylvania 19122, USA*
[2]*Department of Physics and Astronomy and Laboratory for Surface Modification,*
Rutgers University, New Brunswick, New Jersey 08901, USA

(Received 16 August 2022; accepted 16 December 2022; published 26 January 2023)

High-quality, ultrathin superconducting films are required for advanced devices such as hot-electron bolometers, superconducting nanowire single-photon detectors, and quantum applications. Using hybrid physical-chemical vapor deposition, we show that MgB_2 films as thin as 4 nm can be fabricated on the carbon-terminated 6*H*-SiC (0001) surface with a superconducting transition temperature above 33 K and a rms roughness of 0.7 nm. Remarkably, the film quality is a function of the SiC surface termination, with the C-terminated surface preferred to the Si-terminated surface. To understand the MgB_2 thin film/SiC substrate interactions giving rise to this difference, we characterized the interfacial structures using Rutherford backscattering spectroscopy/channeling, electron-energy-loss spectroscopy, and x-ray photoemission spectroscopy. The MgB_2/SiC interface structure is complex and different for the two terminations. Both terminations incorporate substantial unintentional oxide layers influencing MgB_2 growth and morphology, but with a different extent, intermixing, and interface chemistry. In this paper, we report measurements of transport, resistivity, and the critical superconducting temperature of MgB_2/SiC that are different for the two terminations, and they link interfacial structure variations to observed differences. The result shows that the C face of SiC is a preferred substrate for the deposition of ultrathin superconducting MgB_2 films.

DOI: 10.1103/PhysRevMaterials.7.014803

I. INTRODUCTION

Ultrathin superconducting films of MgB_2 have attracted much interest [1–4] due to their relatively high T_c of 39 K, large coherence lengths, and high critical current density [5,6] for applications in bolometers, photon detectors, and quantum devices [7–9]. High-quality MgB_2 films have been fabricated successfully using hybrid physical-chemical vapor deposition (HPCVD) [10], creating thin films with high T_c and low residual resistivity. However, the Volmer-Weber-like island growth mode in the HPCVD process is detrimental to the production of ultrathin and smooth MgB_2 films [11–14], where coalescence of islands often leads to rough surfaces. For many superconducting electronic applications, ultrathin (∼5 nm), smooth (ideally with RMS roughness < 1 nm), and uniform films are required. Previously, we reported on low-angle ion milling to thin 40 nm HPCVD MgB_2 films and fabricated 5 nm superconducting films with T_c as high as 36 K [2]. Novoselov *et al.* have reported growth of 10 nm HPCVD MgB_2 films directly on the Si-terminated SiC (0001) substrate with T_c as high as 35 K [15]. Recently, we have found that ultrathin MgB_2 films grown on C-terminated 6*H*-SiC substrate (0001 bar) are significantly smoother than those on Si-terminated substrates, and they possess high-quality electronic properties and high T_c [16].

Interfacial phenomena are critically important in the design and manipulation of thin-film functional materials [17–20]. Polarity of substrate is one of the important parameters determining the structural, electric, and magnetic properties of materials grown on polar materials. The polarity of SiC has been proved to have a significant influence on the growth as well as the properties of thin films such as graphene, GaN, and AlN thin films [21–23]. Here, we report a comprehensive characterization of ultrathin HPCVD MgB_2 films grown on SiC substrates with both Si- and C-termination. The interface characteristics are correlated with measurements of MgB_2 transport, resistivity, and critical superconducting temperature comparing growth on these two principal SiC faces. A significant finding is the existence of a substantial magnesium oxide layer at the MgB_2/SiC interface with thickness and roughness dependent on the termination of the SiC substrate. The MgO_x layer is thinner and smoother on the C-face than on the Si-face. The smoother MgO_x layer leads to a smoother MgB_2 ultrathin film on the C-face. Overall, the result shows that the C face is a preferred substrate for the deposition of ultrathin superconducting MgB_2 films on SiC. To our knowledge, these MgB_2 films are at the leading edge of this technology, combining the requirements of high T_c, thickness, and uniformity for advanced applications. The interface characterization reported here provides details and possible explanations for the growth habit, and it suggests procedures broadly applicable to superconducting thin-film growth.

II. EXPERIMENTAL DETAILS

SiC substrates used were the 6*H* polytype in the (0001) or $(000\bar{1})$ direction. As described in Ref. [16], a double-side

---

[*] Corresponding author: weibing.yang@temple.edu

[†] These authors contributed equally to this work.

polished 6*H*-SiC(0001) substrate is C-terminated on one side and Si-terminated on the other, leading to surfaces of different polarities. Details of the HPCVD method for growing MgB_2 thin films have been described previously [10]. The HPCVD growth condition has been optimized to minimize the RMS roughness (a flow rate of 10 sccm diborane gas mixture, 5% B_2H_6 in H_2, was used in this work as compared to 2 sccm in our previous work [16]) (see Sec. I of the Supplemental Material [24]). Transport properties of MgB_2 films were characterized by standard four-point measurements [25] where probes were placed in the four corners of 5×5 mm^2 square sample. Resistivity versus temperature measurement was carried out by dipping the sample into a liquid helium dewar immediately after removal from the HPCVD system to minimize air exposure. The measured resistance is converted into resistivity based on the van der Pauw solution for the square-shaped sample [26].

Atomic force microscopy (AFM), scanning transmission electron microscopy (STEM), x-ray photoelectron spectroscopy (XPS), and Rutherford backscattering spectrometry (RBS) were used to characterize the film and the interface. AFM measurements were performed using a Veeco atomic force microscope. Imaging and electron-energy-loss spectroscopy were carried out using the Rutgers Nion UltraSTEM microscope operated at 60 kV with the convergence and collection semiangles at 35 and 16.5 mrad, respectively. XPS measurements were performed in a Thermo K-alpha system with charge compensation using Al $K\alpha$ radiation and an overall energy resolution of 0.7 eV. Under these conditions, the surface hydrocarbons were found at a binding energy of 284.7 eV. RBS measurements were performed using a General Ionex tandem accelerator with 1.6 MeV He^{++} ions and a scattering angle of 130°. The sample was held approximately normal to the ion beam. The estimated depth resolution for Mg is ~ 25 nm. Ion beam channeling was performed along the (0001) direction of the 6H-SiC substrate, and nonchanneling (random) spectra were acquired by randomly varying incident angles. SIMNRA 7.01 software was used for nonchanneling RBS spectra analysis [27].

III. RESULTS

A. Deposition rates and surface roughness

As described in detail in the Supplemental Material [24], the basic growth method involves liquified Mg combined with a flow of diborane gas to form MgB_2. In previous work [16], we used flow rates of 1 and 2 sccm diborane gas mixture in the HPCVD deposition, and we obtained an RMS roughness of 1.2 nm and T_c of 34.3 K in a 5.7 nm MgB_2 thin film on the C face of the SiC substrate. From a more recent systematic optimization of the diborane gas mixture flow rate, we found that 10 sccm produces the smallest roughness with the best superconducting properties. Figure 1 shows AFM images of MgB_2 thin films with nominal thicknesses of 4, 9, 16, and 22 nm grown on the Si and C faces. Films with the same thickness but different terminations were grown in the same deposition run to ensure identical growth conditions. For all thicknesses, films on the C face are smoother than those on the Si face. Films on the Si face show clusters that are absent on the films on the C face. Energy-dispersive x-ray spectroscopy (EDS) analysis shows that the clusters are MgB_2 grains. In addition, the films on the Si face show taller islands that are not completely connected, while films on the C face show much better connectivity. On the Si face, the MgB_2 islands become larger for thicker depositions, typical for the island growth. Films of the same nominal thickness on the C face show a much smoother surface and do not have typical hexagonal MgB_2 grains as the case on the Si face. The RMS roughness for the MgB_2 films in Fig. 1 is summarized in Table I, showing values from 0.5 to 0.7 nm for the C face and 2–3 nm for the Si face. The result is a marked improvement over those in Ref. [16], and it indicates that MgB_2 films grown on the C face can be smoother than those grown on the Si face. Films composed of grains with a size comparable to the total film thickness are intuitively rougher.

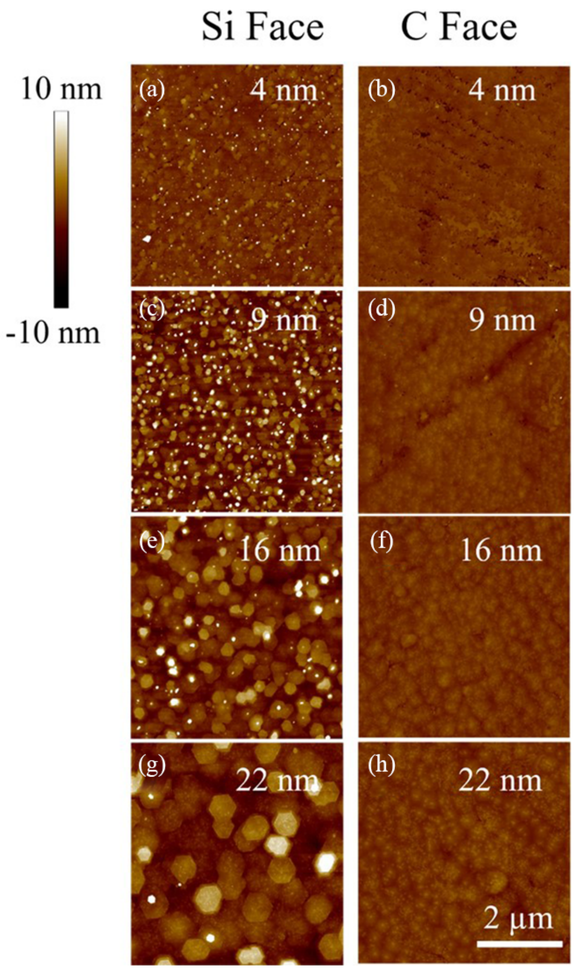

FIG. 1. (a), (c), (e), and (g) AFM images for MgB_2 films grown on Si-terminated SiC with thicknesses of 4, 9, 16, and 22 nm, respectively; (b), (d), (f), and (h) are the corresponding MgB_2 films on the C-terminated SiC that were grown under the same conditions as (a), (c), (e), and (g).

B. Electronic properties

Figure 2 shows corresponding resistivity versus temperature (ρ-T) curves for the MgB_2 films in Fig. 1. As the film thickness decreases, T_c decreases and the residual resistivity

TABLE I. RMS roughness, T_{c0}; residual resistivity, ρ_0; and $\Delta\rho$ of MgB_2 films on C-SiC and Si-SiC.

Film thickness (nm)		4	9	16	22
C face	RMS (nm)	0.7	0.6	0.5	0.7
	T_{c0} (K)	33.6	37.5	39.4	39.8
	ρ_0 ($\mu\Omega$ cm)	14.9	4.9	1.9	1.3
	$\Delta\rho$ ($\mu\Omega$ cm)	14.2	10.6	8.3	7.5
Si face	RMS (nm)	1.7	3.2	2.9	2.7
	T_{c0} (K)	35.4	37.8	39.2	40.6
	ρ_0 ($\mu\Omega$ cm)	24.7	5.3	2.3	1.4
	$\Delta\rho$ ($\mu\Omega$ cm)	24.3	10.6	8.1	7.7

ρ_0 increases for films on both the Si and C faces. The T_c of MgB_2 films on the Si face is slightly higher than that of the films on the C face, which is probably due to the biaxial tensile strain between MgB_2 grains, as the MgB_2 growth mode on the Si face is more like island growth mode compared to the C face [28]. The results are summarized in Table I. While the values of T_c are similar to our earlier report [16], the ρ_0 values of the current films are much lower. The results are similar for both substrate terminations except for the thinnest films. The residual resistivity is much higher for the 4 nm film on the Si face than on the C face.

Also included in Table I is $\Delta\rho$, the change in resistivity from room temperature to just above the superconducting transition temperature. Rowell has shown that this quantity, the room temperature, and the residual resistivity difference can be used to quantify the grain connectivity in MgB_2 samples [29], with larger $\Delta\rho$ indicating poorer connectivity. The dependence of $\Delta\rho$ on film thickness is shown in Fig. 3(a). At 22 nm, the films on both Si and C faces show $\Delta\rho$ values similar to our thicker, high-quality MgB_2 films, indicating excellent grain connectivity. As the nominal thickness of the ultrathin film decreases, the grain connectivity effect becomes more and more important, reflected as a gradual increase in $\Delta\rho$. At 4 nm, the connectivity degrades rapidly, leading to a large $\Delta\rho$ increase for both faces. The film on the Si face shows much poorer connectivity than that on the C face. The conclusion on the grain connectivity is corroborated by the residual resistivity data. While $\Delta\rho$ reflects the temperature dependence of the electron-phonon scattering and grain connectivity, ρ_0 is determined by the grain connectivity and scattering of electrons by impurities, defects, as well as surfaces [29]. We have shown previously [30] that for clean MgB_2 films fabricated by HPCVD, the mean free path of electron scattering is limited by the film thickness. For example, changing the film thickness from 22 to 4 nm results in a decrease in the mean free path and thus an increase in electron scattering by a factor of 5.5. Combined with a reduction of grain connectivity, deduced from the increase in $\Delta\rho$, by a factor of 1.9 in the case of films on the C face, one can predict the ρ_0 value of the 4 nm film from that of the 22 nm film. The result, $\rho_0 = 1.3 \times 5.5 \times 1.9 = 13.7$ $\mu\Omega$ cm for the 4 nm film, agrees well with the experimentally measured value. The results of the same procedure for all the films studied are shown in Figs. 3(b) and 3(c).

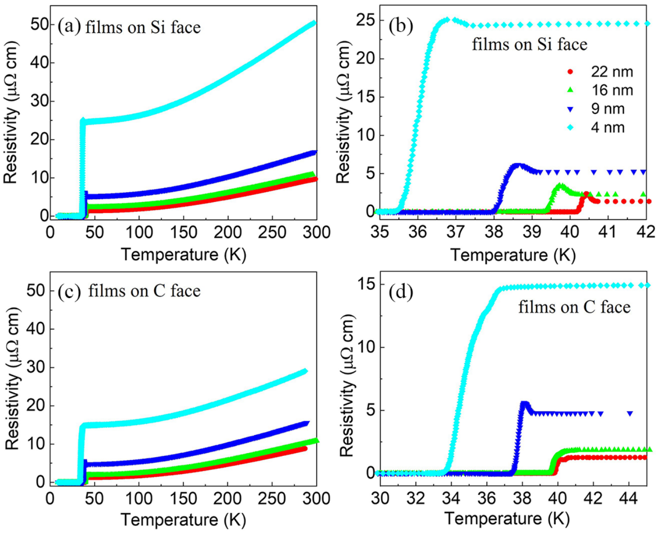

FIG. 2. Resistivity vs temperature curves for MgB_2 films on the Si face (a), (b) and the C face (c), (d).

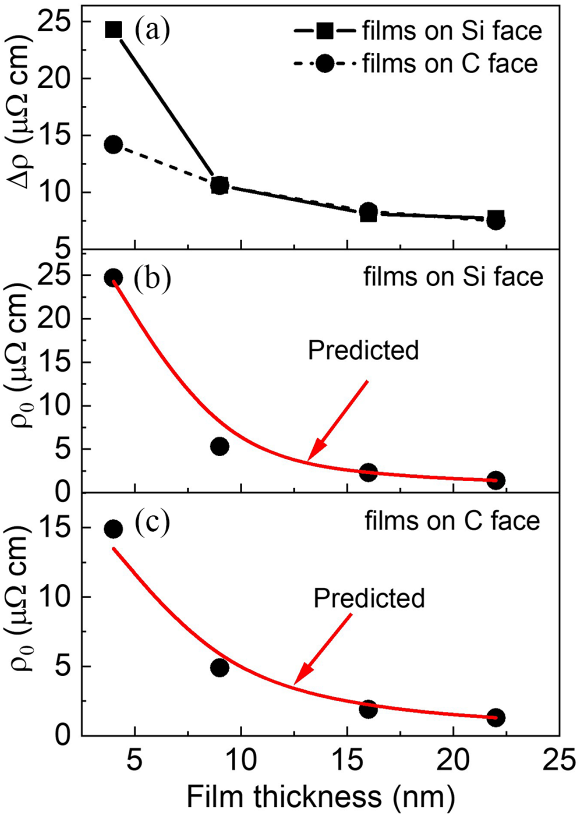

FIG. 3. The change of resistivity from 300 to 40 K and residual resistivity as a function of film thickness on both the Si and the C face. The red curves are values expected based on the reductions of the electron mean free path and the grain connectivity as the film thickness decreases.

C. Interface characterization

To understand the influence of the SiC surface termination on the properties of ultrathin MgB_2 films, we investigated

TABLE II. Atomic composition of MgB_2/SiC determined by RBS.

$MgB_2/MgO_x/SiC$	$O_{interface}/cm^2$ ($\times 10^{15}$)	$Mg_{interface}/cm^2$ ($\times 10^{15}$)	Thickness of MgO_x interface (nm)
Si face (Ch-RBS)	13 ± 2	12 ± 2	2.3 ± 0.2
C face (Ch-RBS)	6 ± 2	4 ± 2	0.9 ± 0.2

the interfacial structure and chemistry of the MgB_2/SiC interface. The MgB_2 samples for interface characterizations are prepared separately using the same growth conditions as were used for the films described above to ensure that the properties of MgB_2 films are consistent throughout this work.

1. RBS channeling and interfacial oxides

RBS/channeling measurements were performed to provide depth-dependent information on both the composition ("random spectra") and crystallinity. Channeling, the reduction of scattering yield when the beam is aligned with a major crystallographic direction, yields information on crystal quality and identifies the alignment and composition of buried layers. The results show that for both SiC terminations, there is clearly an interfacial layer between the MgB_2 film and the SiC substrate containing both magnesium and oxygen (see Sec. II of the Supplemental Material [24]). The result of a composition analysis at the interface for the two samples, identified as $MgB_2/MgO_x/SiC$, is presented in Table II, where the interfacial oxygen is ascribed to a MgO_x layer. Within the experimental error, the composition of the interfacial layer is close to MgO. The thickness of the MgO_x layer is estimated to be ∼2.3 nm for the Si termination and ∼ 0.9 nm for the C termination. Furthermore, there is a consistent, but small, channeling effect in the MgO_x itself, indicating that the oxide is crystalline. We suggest that the Mg-interface peaks result from a partially crystalline MgO layer at the interface, with orientation affected by the lattice mismatch between MgO and SiC, and then influenced by the mismatch with overlayer MgB_2 and MgO_x. (RBS also detected monolayer-scale surface impurities of silicon and carbon at the surface of the MgB_2 overlayer that play no apparent role in the interface formation, but they are noted here for completeness.) The observation of a substantial oxide interfacial layer is a major new finding. The "buried oxide" is shown to be consistent with magnesium oxide by the chemical shift as observed in angular-dependent high-energy XPS (HAXPES) analysis (see Sec. III of the Supplemental Material [24]; also see Refs. [31–37] therein).

The observation of a MgO_x interfacial layer raises two questions: (i) Since the HPCVD process, being entirely conducted in a reducing environment, in principle eliminates the oxygen from the film growth, what is the origin of the oxygen? (ii) What role does the oxide layer play in determining the properties of the ultrathin MgB_2 films associated with different terminations? To address these questions, we investigated the first stages of the HPCVD process itself by heating the substrate along with the Mg pieces, without the introduction of the B_2H_6 gas mixture. Specifically, Si- and C-terminated SiC substrates were heated in Mg vapor at 740 °C for 1 min.

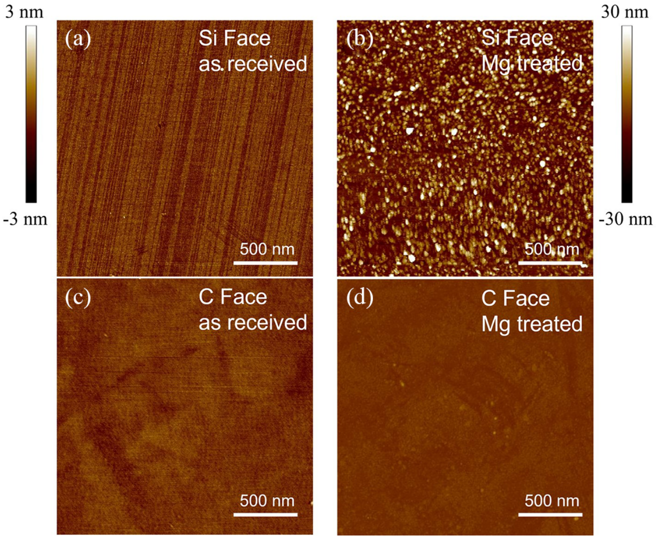

FIG. 4. (a) Atomic force microscopy (AFM) of Si-SiC as received from the vendor, (b) AFM image of Si-SiC after annealing in Mg vapor at 740 °C for 1 min, (c) AFM scan for C-SiC as received from the manufacturer, and (d) AFM image of C-termination of SiC after annealing in Mg vapor at 740 °C for 1 min.

In Fig. 4, AFM images of these treated Si- and C-terminated SiC substrates are shown along with those for the pristine substrates as received from the vendor. For the "as-received" material, the Si-terminated surface [Fig. 4(a)] shows atomic steps with an RMS roughness of 0.2 nm, whereas the C-terminated surface [Fig. 4(c)] is featureless with an RMS roughness of ∼0.3 nm. Following the "Mg-only" treatment, the samples are essentially MgO/SiC structures due to oxidation of the air-exposed Mg layer. The roughness measured on Si-terminated substrate is much higher (RMS roughness ∼4 nm) than that measured on the C-terminated substrate (RMS roughness ∼0.4 nm). The samples consistently show an oxygen-rich layer with an Mg:O ratio of ∼1 : 1.3 for both surface terminations and a small channeling effect indicative of imperfect or misaligned MgO crystallinity. The MgO_x layer is thicker on Si-SiC (3.0 ± 0.2 nm as determined from the channeling spectrum) than on C-SiC: (2.1 ± 0.2 nm). Note that both layers are thicker than the MgO_x layers detected at the MgB_2/SiC interface: 2.3 ± 0.2 nm on the Si face and 0.9 ± 0.2 nm on the C face, due to further oxidation upon air exposure.

2. STEM electron energy loss spectroscopy and nm elemental profiling

To further examine the interface between the MgB_2 films and the underlying C- and Si-terminated SiC substrates, cross-section samples were prepared and studied by STEM-EELS. As shown in the atomic resolution HAADF images in Fig. 5, there is an intermediate layer between the top MgB_2 and the bottom SiC for both terminations. This interface layer is about 0.9 nm in both cases. However, while not shown here, the intermediate layer does not have constant thickness across the observed interface ranges, and it varies from 0.9 to 2.7 nm for the case of Si-SiC and from 0.9 to 1.8 nm for the case of C-SiC. In addition, the intermediate layer marked with dashed

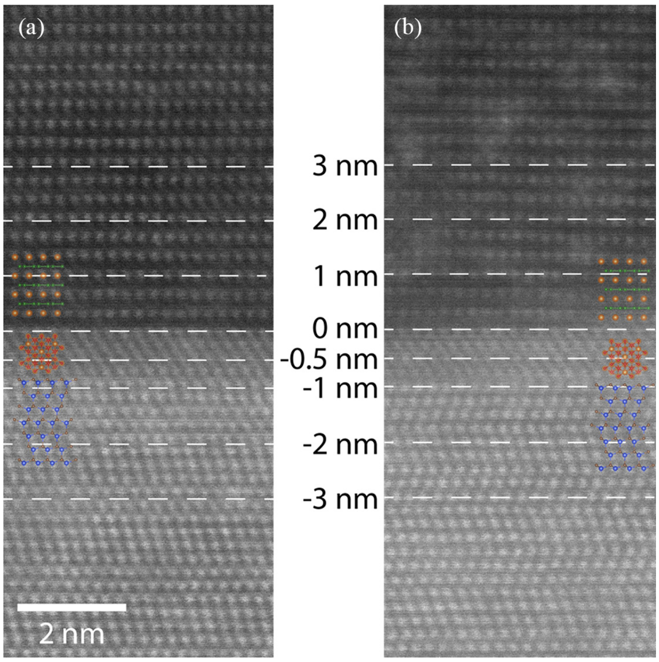

FIG. 5. Cross-sectional HAADF STEM imaging of MgB_2 on (a) C-terminated SiC(0001) substrate, and (b) Si-terminated SiC(0001) substrate.

lines between 0 and −1 nm in both cases often exhibits a periodic structure as shown in the figure. Even though the resolution of the STEM image for the MgO layer is not ideal due to the combination of limited resolution of our instrument and the complex and imperfect thin structure, we can still see that the structure matches well with MgO as viewed from the (111) direction. The atomic arrangements of MgB_2, MgO, and SiC are overlaid in the figure as visual guides. Note that the image intensity scales with the atomic number due to the detector arrangement, and it is Mg and Si observed in MgB_2 and SiC, respectively.

Next, we compare the relative chemical distributions of Mg, Si, B, C, and O along the eight data points acquired across the interface areas in Fig. 6. It is found that oxygen is mostly confined in the intermediate layer. Si and C are found to terminate near the intermediate layer, as expected, whereas B is found on the thin film/surface side of the intermediate layer. Finally, Mg is found throughout the intermediate layer, consistent with a MgO interface.

3. XPS analysis and interfacial chemistry

More detailed information on interfacial chemistry is revealed by XPS. Figure 7 shows selected core-level spectra (Mg 1*s*, Si 2*p*, O 1*s*, and C 1*s*) measured on bare SiC substrates (bottom curves), Mg vapor treated SiC (middle curves), and 7-nm-thick MgB_2 grown on SiC (top curves), for both Si- and C-terminated surfaces. In all cases, the SiC substrate signal is detectable via the Si 2*p* and C 1*s* core levels. Chemical environments attributed to core-level features are indicated in the figure. On the bare SiC surface, exposed to air after preparation, the substrate Si 2*p* and C 1*s* core levels are found at binding energies of ∼100 and ∼282 eV, respectively, in good agreement with expected values [38]. The features in the O 1*s* and C 1*s* core-level spectra indicate carbohydrate adsorption, the result of air exposure of the bare SiC substrates.

For the Mg vapor treated SiC samples, the O 1*s* level is split into two peaks. The lower binding-energy component is attributed to MgO while the higher binding-energy component is assigned to $Mg(OH)_x$ and Mg carbonates [39]. Of particular interest is the fact that the SiC-related core-level spectra show different binding energies for the two different SiC surface terminations: the binding energies of both the C 1*s* and Si 2*p* core levels are ∼ 1 eV lower for the C face than for the Si face. For MgB_2 films on SiC substrate, exposure to air causes surface oxidation as well as water and carbohydrate adsorption. As a result, their O 1*s* and Mg 1*s* spectra are affected by both the top surface alteration of MgB_2 and the interfacial MgO_x layer, and separating these contributions is not straightforward. However, we again observe a shift of the Si 2*p* core level to lower binding energy by ∼1 eV in the sample on the C face as compared to the Si face (a similar energy shift is present for C 1*s*, but less visible due to the SiC signal attenuation through the MgB_2 layer). This suggests that in the cases of both Mg vapor treated SiC (for which the stack is effectively MgO/SiC) and MgB_2 films on SiC (for which the stack is likely MgB_2/MgO/SiC), there is a similar energy alignment related to the MgO/SiC interface that is dependent on the SiC surface termination. Similar behavior has been reported in the case of intentionally grown epitaxial MgO films on SiC surfaces [40,41]: binding-energy offsets of the order

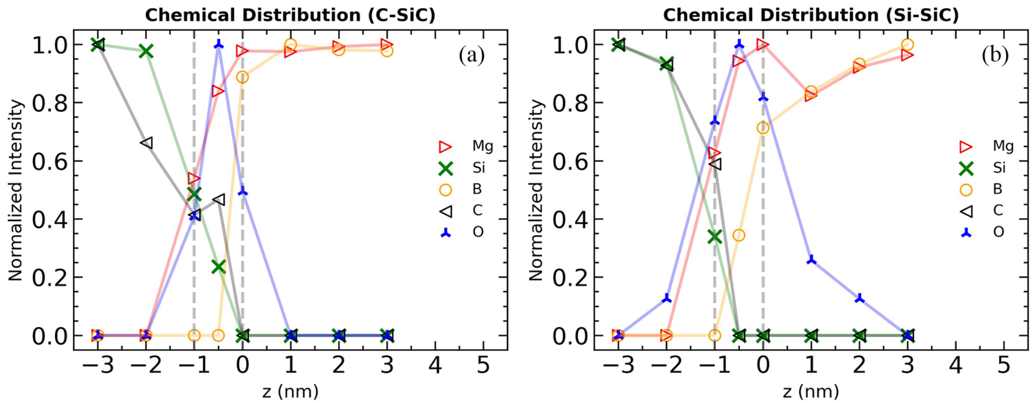

FIG. 6. STEM-EELS data from the same cross section for (a) C-terminated SiC(0001) substrate, and (b) Si-terminated SiC(0001) substrate.

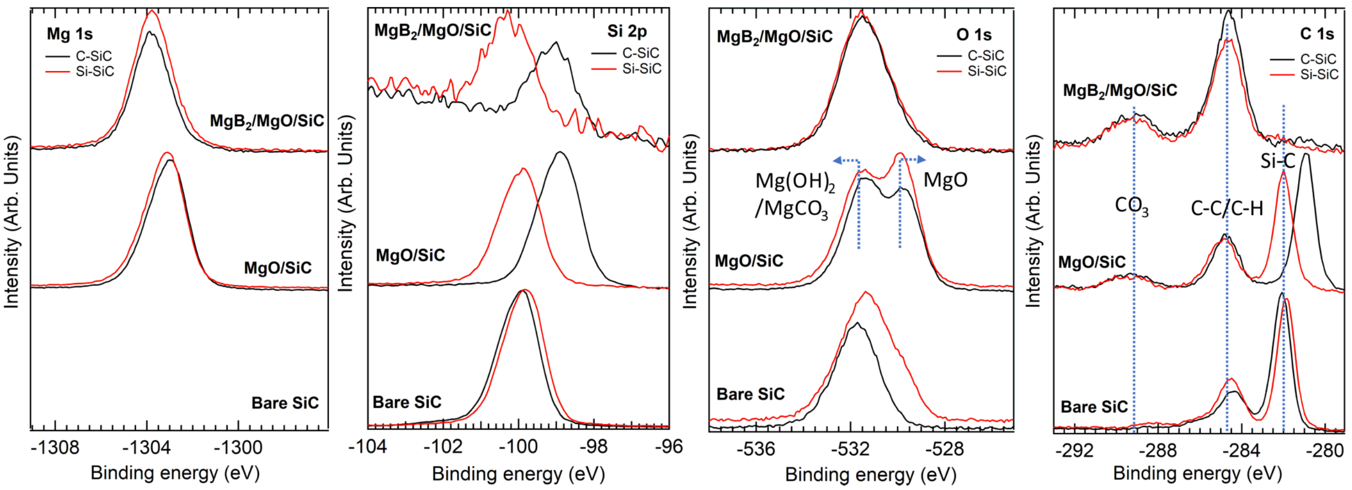

FIG. 7. XPS spectrum of Mg 1*s*, Si 2*p*, O 1*s*, and C 1*s* for bare SiC, Mg vapor treated SiC, and thin MgB_2 film on SiC for both C and Si terminations.

of electron volts have been measured for different MgO/SiC interfaces, supported by electronic structure calculations of atomically different interfaces.

IV. DISCUSSION

In this section, we consider specific aspects of these analyses and how they might influence the film morphology.

It is clear from the different interface analysis results above that a buried MgO layer exists at the interface of the MgB_2 film and the SiC substrate. It is likely that this oxide is the result of the reaction of Mg with the "native oxide" that exists on the SiC surface. The reaction of Mg with SiO_2 has been reported by a number of authors, who suggest that the reaction can result in the formation of MgO and possibly Mg silicates [42,43].

"Native oxide" as a thin film is not necessarily well-defined, as the resulting oxide thickness, usually only 1–2 nm at most, is a result of environmental variables, time, and the crystal face. In recent work using contact angle measurements, Kim *et al.* [44] showed that the native oxide growth is greater on the Si face than on the carbon face, consistent with the reports in Table II of a Si-face MgO layer of 2.3 nm compared to a C face of 0.9 nm. For calibration, we note that 1 nm of SiO_2 corresponds to $5.3 \times 10^{15}/\mathrm{cm}^2$ of oxygen, consistent with the existence of very thin native oxides yielding nanometer MgO. Furthermore, Nagai *et al.* [45] characterized the roughness in very thin oxides on SiC as a function of the crystal face. In this work, the authors show that the RMS roughness is proportional to oxide thickness, and the rate of increase of roughness with film thickness is the same for the two crystal faces. Therefore, the Si-face oxide roughness is greater than that of the C face. These reports allow some mechanistic conclusions, as follows: Native oxide thickness on the C face is less than that of the Si face [44], consistent with the reports in Table II. The roughness of very thin oxides is proportional to oxide thickness [45]. In short, oxide roughness is proportional to oxide thickness, and this oxide roughness is transferred to a MgO layer and then reflected in the overlayer MgB_2 film uniformity. Since the C-face oxide is substantially less than the Si face oxide, the net roughness is reduced for the C face, resulting in a more uniform thin film.

Relevant to that point, it is interesting to note that there are reports of the growth of MgO on SiC by MBE for MOS systems [46,47], a good lattice match, and there are reports of the growth of MgB_2 on MgO [48], also a reasonable lattice match resulting in high-quality MgB_2 films. Therefore, an MgB_2/MgO/SiC epitaxial structure may be realized. Nevertheless, the properties of the resulting film may depend on the SiC termination: if the starting (oxidized) surface of the C face of SiC is less rough than that of the Si face, a smoother MgO/MgB_2 structure is expected.

Finally, among the interesting remaining questions is the "necessity" for a magnesium-based oxide layer to achieve higher-quality epitaxy and crystallinity. This point was explicitly raised in the MBE work of Laloe *et al.* [49] for MgB_2 on Si where a Mg starting layer was explicitly added to enhance growth. The "native oxide" on the Si face may be just the correct amount to achieve a high-quality epitaxial film. In that regard, we note that some preliminary experiments on HF-treated SiC (presumably minimal oxide) in our laboratory did not produce quality films.

V. CONCLUSION

The growth of ultrathin MgB_2 films on the different surface terminations of SiC has been studied, seeking the conditions for optimum superconducting properties and film uniformity. It has been shown that the best conditions are associated with 10 sccm of 5% diborane gas flow rate on the C-terminated face of SiC for our specific system. A significant difference has been identified between growth on the Si face and the C face, with the latter producing higher-quality films. This difference has been explored by various interface probes.

RBS/channeling measurements indicated that the samples consisted of MgB_2/MgO/SiC stacks, in which the thickness of the MgO_x layer was SiC surface termination-dependent: it is 2.3 ± 0.2 nm on the Si face and 0.9 ± 0.2 nm on the C face. High-resolution EELS and TEM confirmed this structural difference, indicating that different interfacial constituents on the two surfaces may control the final morphology. XPS analysis indicated a similar energy band offset at the MgO/SiC interfaces, for both MgB_2 films grown on SiC and for MgO films on SiC, but highly dependent on the SiC surface termination. High-energy, grazing exit angle XPS confirmed the presence of a buried, thin MgO_x layer at the MgB_2/SiC interface.

This MgO layer in turn may govern the MgB_2 film quality: a thicker and rougher MgO_x layer on the Si face of the SiC substrate is the cause of the rougher ultrathin MgB_2 films as compared to the films on the C face of SiC. The achievement of such high-quality superconducting films, and the knowledge of the parameters that control their growth, maybe a precursor to new devices and device configurations employing their unique electronic properties.

ACKNOWLEDGMENTS

Research at Temple University was supported by NASA's Astrophysics Research and Analysis Program through a contract from JPL (Contract No. 1632463). Research at Rutgers was supported by Laboratory for Surface Modification (LSM). A.X.G., R.K.S., and J.R.P. acknowledge support from the DOE, Office of Science, Office of Basic Energy Sciences, Materials Sciences, and Engineering Division under Award No. DE-SC0019297. The electrostatic photoelectron analyzer for the lab-based HAXPES measurements at Temple University was acquired through an Army Research Office DURIP grant (Grant No. W911NF-18-1-0251).

[1] Y. Zhang, Z. Lin, Q. Dai, D. Li, Y. Wang, Y. Zhang, Y. Wang, and Q. Feng, Supercond. Sci. Technol. **24**, 015013 (2010).

[2] N. Acharya, M. A. Wolak, T. Tan, N. Lee, A. C. Lang, M. Taheri, D. Cunnane, B. S. Karasik, and X. X. Xi, APL Mater. **4**, 086114 (2016).

[3] B. S. Karasik, M. C. Gaidis, W. R. McGrath, B. Bumble, and H. G. LeDuc, Appl. Phys. Lett. **71**, 1567 (1997).

[4] H. Shimakage, M. Tatsumi, and Z. Wang, Supercond. Sci. Technol. **21**, 095009 (2008).

[5] J. Nagamatsu, N. Nakagawa, T. Muranaka, Y. Zenitani, and J. Akimitsu, Nature (London) **410**, 63 (2001).

[6] C. Buzea and T. Yamashita, Supercond. Sci. Technol. **14**, R115 (2001).

[7] L. Kasaei, T. Melbourne, M. Li, V. Manichev, F. Qin, H. Hijazi, L. C. Feldman, T. Gustafsson, B. A. Davidson, X. X. Xi, and K. Chen, IEEE Trans. Appl. Supercond. **29**, 5 (2019).

[8] D. Cunnane, J. H. Kawamura, M. A. Wolak, N. Acharya, T. Tan, X. X. Xi, and B. S. Karasik, IEEE Trans. Appl. Supercond. **25**, 1 (2014).

[9] H. Shibata, T. Akazaki, and Y. Tokura, Appl. Phys. Express **6**, 023101 (2013).

[10] X. Zeng, A. V. Pogrebnyakov, A. Kotcharov, J. E. Jones, X. X. Xi, Lysczek, J. M. Redwing, S. Xu, Q. Li, J. Lettieri, D. G. Schlom, W. Tian, X. Pan, and Z. Liu, Nat. Mater. **1**, 35 (2002).

[11] C. Zhang, Y. Wang, D. Wang, Y. Zhang, Z. H. Liu, Q. R. Feng, and Z. Z. Gan, J. Appl. Phys. **114**, 023903 (2013).

[12] Y. Wang, C. Zhuang, X. Sun, X. Huang, Q. Fu, Z. Liao, D. Yu, and Q. Feng, Supercond. Sci. Technol. **22**, 125015 (2009).

[13] M. A. Wolak, N. Acharya, T. Tan, D. Cunnane, B. S. Karasik, and X. X. Xi, IEEE Trans. Appl. Supercond. **25**, 1 (2015).

[14] C. Zhuang, K. Chen, J. M. Redwing, Q. Li, and X. X. Xi, Supercond. Sci. Technol. **23**, 055004 (2010).

[15] E. Novoselov, N. Zhang, and S. Cherednichenko, IEEE Trans. Appl. Supercond. **27**, 7500605 (2017).

[16] W. Yang, K. Chen, D. Cunnane, B. S. Karasik, and X. Xi, IEEE Trans. Appl. Supercond. **32**, 7500204 (2022).

[17] R. U. Chandrasena, W. Yang, Q. Lei, M. U. Delgado-Jaime, K. D. Wijesekara, M. Golalikhani, B. A. Davidson, E. Arenholz, K. Kobayashi, M. Kobata, and F. M. De Groot, Nano Lett. **17**, 2 (2017).

[18] S. Tan, Y. Zhang, M. Xia, Z. Ye, F. Chen, X. Xie, R. Peng, D. Xu, Q. Fan, H. Xu, and J. Jiang, Nat. Mater. **12**, 634 (2013).

[19] S. He, J. He, W. Zhang, L. Zhao, D. Liu, X. Liu, D. Mou, Y. B. Ou, Q. L. Wang, Z. Li, and L. Wang, Nat. Mater. **12**, 605 (2013).

[20] S. Haindl, S. Nikolaev, M. Sato, M. Sasase, and I. MacLaren, NPG Asia Mater. **13**, 67 (2021).

[21] M. Harada, Y. Ishikawa, T. Saito, and N. Shibata, Jpn. J. Appl. Phys. **42**, 2829 (2003).

[22] F. Varchon, R. Feng, J. Hass, X. Li, B. N. Nguyen, C. Naud, P. Mallet, J.-Y. Veuillen, C. Berger, E. H. Conrad, and L. Magaud, Phys. Rev. Lett. **99**, 126805 (2007).

[23] T. Sasaki and T. Matsuoka, J. Appl. Phys. **64**, 4531 (1988).

[24] Supplemental Material at http://link.aps.org/supplemental/10.1103/PhysRevMaterials.7.014803 for more details about experimental methods, RBS/channeling and HAXPES measurements.

[25] L. J. van der Pauw, Philips Res. Rep. **13**, 1 (1958).

[26] M. G. Buehler and W. R. Thurber, Solid State Electron. **20**, 403 (1977).

[27] M. Mayer, in *Proceedings of the 15th International Conference on the Application of Accelerators in Research and Industry*, edited by J. L. Duggan and I. L Morgan (1999), p. 541.

[28] A. V. Pogrebnyakov, J. M. Redwing, S. Raghavan, V. Vaithyanathan, D. G. Schlom, S. Y. Xu, Q. Li, D. A. Tenne, A. Soukiassian, X. X. Xi, M. D. Johannes, D. Kasinathan, W. E. Pickett, J. S. Wu, and J. C. H. Spence, Phys. Rev. Lett. **93**, 147006 (2004).

[29] J. M. Rowell, Supercond. Sci. Technol. **16**, R17 (2003).

[30] X. X. Xi, Supercond. Sci. Technol. **22**, 043001 (2009).

[31] A. X. Gray, C. Papp, S. Ueda, B. Balke, Y. Yamashita, L. Plucinski, J. Minár, J. Braun, E. R. Ylvisaker, C. M. Schneider, and W. E. Pickett, Nature Mater. **10**, 759 (2011).

[32] A. Jablonski and C. J. Powell, J. Vac. Sci. Technol. A **27**, 253 (2009).

[33] C. S. Fadley, Prog. Surf. Sci. **16**, 275 (1984).

[34] H. Li, J. Zhu, Z. Wang, Z. Song, and H. Chen, Optical Mater. Express **3**, 546 (2013).

[35] M. Niwa, A. Yasui, E. Ikenaga, H. Honjo, S. Ikeda, T. Nakamura, and T. Endoh, J. Appl. Phys. **125**, 203903 (2019).

[36] G. Panaccione and K. Kobayashi, Surf. Sci. **606**, 125 (2012).

[37] W. Smekal, W. S. M. Werner, and C. J. Powell, Surf. Interface Anal. **37**, 1059 (2005).

[38] M. J. Bozack, Surf. Sci. Spectra **3**, 1 (1994).

[39] V. Fournier, P. Marcus, and I. Olefjord, Surf. Interface Anal. **34**, 494 (2002).

[40] D. J. Pingstone, Ph.D. thesis, University of York (2018).

[41] B. L. Zhang, F. F. Cai, G. S. Sun, H. B. Fan, P. F. Zhang, H. Y. Wei, X. L. Liu, S. Y. Yang, Q. S. Zhu, and Z. G. Wang, Appl. Phys. Lett. **93**, 072110 (2008).

[42] T. Henmi, T. Shiono, K. Matsubara, T. Kiyomura, H. Kurata, T. Wakasugi, A. Okada, and K. Kadono, Intl. J. Ceramic Eng. Sci. **2**, 2 (2020).

[43] P. Casey and G. Hughes, J. Appl. Phys. **107**, 074107 (2010).

[44] J. G. Kim, W. S. Yoo, J. Y. Park and W. J. Lee, ECS J. Solid State Sci. Technol. **9**, 12 (2020).

[45] R. Nagai, R. Hasunuma, and K. Yamabe, Jpn. J. Appl. Phys. **55**, 08PC07 (2016).

[46] T. L. Goodrich, J. Parisi, Z. Cai, and K. S. Ziemer, Appl. Phys. Lett. **90**, 042910 (2007).

[47] T. L. Goodrich, Z. Cai, and K. S. Ziemer, Appl. Surf. Sci. **254**, 10 (2008).

[48] Y. Harada, M. Uduka, Y. Nakanishi, N. Yoshimoto, and M. Yoshizawa, Physica C **412**, 1383 (2004).

[49] J.-B. Laloë, T. H. Kim, and J. S. Moodera, Adv. Condens. Matter Phys. **2011**, 989732 (2011).